

Geophysical Research Letters®

RESEARCH LETTER

10.1029/2025GL116436

Seismic Velocity Variations, Ground Deformation and the Role of Fluids During a Low-Energy Seismic Swarm



Key Points:

- We exploit a dense near-fault observational network of seismo-geodetic instruments to resolve faint signals of a low energy $M_w \leq 4.5$ swarm
- We report on the crustal damaging associated with the earthquakes and we infer possible fluids related effects in enhancing such damaging
- We model the deformation and pore pressure between the two largest events, comparing it with the measurements at borehole strainmeter sites

Supporting Information:

Supporting Information may be found in the online version of this article.

Correspondence to:

E. Mandler,
eugenio.mandler@ingv.it

Citation:

Mandler, E., Zaccarelli, L., Nespole, M., Belardinelli, M. E., Pintori, F., Serpelloni, E., et al. (2026). Seismic velocity variations, ground deformation and the role of fluids during a low-energy seismic swarm. *Geophysical Research Letters*, 53, e2025GL116436. <https://doi.org/10.1029/2025GL116436>

Received 18 APR 2025

Accepted 21 NOV 2025

Author Contributions:

Conceptualization: Eugenio Mandler, Lucia Zaccarelli, Massimo Nespole, Maria Elina Belardinelli, Enrico Serpelloni, Adriano Gualandi









Data curation: Eugenio Mandler

Writing – original draft:

Eugenio Mandler

Writing – review & editing:

Eugenio Mandler, Lucia Zaccarelli, Massimo Nespole, Maria Elina Belardinelli, Francesco Pintori, Enrico Serpelloni, Adriano Gualandi, Lauro Chiaraluca

Eugenio Mandler¹ , Lucia Zaccarelli¹ , Massimo Nespole² , Maria Elina Belardinelli² , Francesco Pintori¹ , Enrico Serpelloni¹ , Adriano Gualandi³ , and Lauro Chiaraluca⁴ 

¹Istituto Nazionale di Geofisica e Vulcanologia (INGV), Bologna, Italy, ²Dipartimento di Fisica e Astronomia “Augusto Righi”, Alma Mater Studiorum Università di Bologna, Bologna, Italy, ³Department of Earth Science, University of Cambridge, Cambridge, UK, ⁴Istituto Nazionale di Geofisica e Vulcanologia (INGV), Roma, Italy

Abstract On March 9th, 2023, three small earthquakes ($3.8 \leq M_w \leq 4.5$) occurred near Umbertide (Central Italy), within 4 hours. Analyzing seismic ambient noise in the frequency band 0.1–1 Hz from six seismometers within 20 km of the M_w 4.5, we detect a significant drop in seismic velocity at the time of occurrence of the seismic sequence. A strain sensitivity analysis suggests that crustal damage was primarily caused by the passage of seismic waves, likely enhanced by the presence of fluids. Analyzing geodetic data from recently installed strainmeters and pore pressure transducers, we highlight the role of elastic strain and fluids in driving deformation during this sequence, suggesting the presence of a pressure source that strongly influences the deformation pattern. We find that fluid-induced stress may cause the reloading of a few kPa of a co-seismic asperity within hours, unveiling the contribution of pore pressure sources to the stress budget of seismogenic faults.

Plain Language Summary On March 9, 2023, a sequence of small earthquakes ($M_w \leq 4.5$) occurred in the northern Apennines (Italy). Although the events were relatively small, we observed a clear and sudden reduction in the speed of seismic waves traveling through the Earth's crust. This drop is a sign of physical changes in the rocks, likely caused by the shaking of the earthquakes and the presence of underground fluids. We combined data from seismic sensors, strainmeters, and instruments that measure underground water pressure. Together, these observations showed that underground fluids may have amplified the effects of the earthquakes and contributed to how the ground moved afterward. The data also suggest that fluids may have moved more easily through the crust after the shaking, changing the pressure conditions in ways that might help trigger further seismic activity. Our findings show that even small earthquakes can cause important changes underground when fluids are involved. Monitoring these changes using a mix of seismic and geodetic tools helps scientists better understand how earthquakes work and how fluid-filled faults behave.

1. Introduction

On March 9th 2023 three earthquakes nucleated near the town of Umbertide in the Umbria-Marche Apennines, Central Italy, with magnitudes $M_w \in [3.8; 4.5]$ (Figure 1). The sequence began at 15:05 UTC with a M_w 4.3 event, followed by the largest M_w 4.5 earthquake at 19:08 UTC, and a M_w 3.8 5 min later. The tectonics of this Apennine sector are shaped by a complex normal fault system formed during the Quaternary extensional phase, overprinting earlier Miocene-Pleistocene compressional structures (Anderlini et al., 2016). Active NE-SW extension at $\sim 2-3$ mm/yr (Serpelloni et al., 2022) is accommodated by normal faults, specifically in this area by the E-dipping low angle Alto Tiberina Fault (ATF) and associated splay faults (Anderlini et al., 2016; Pauselli et al., 2006; Vadacca et al., 2016). Stress build up produced by the creep of the ATF can be released by both aseismic (e.g., Gualandi et al., 2017) and seismic (e.g., Anderlini et al., 2016) events on the ATF synthetic and antithetic splay faults, highlighting the importance of investigating the typical small seismic swarms ($M_w < 4.5$) of this area (Valoroso et al., 2017).

The March 9th events nucleated at shallow depths ($\sim 3-5$ km) within a fractured crustal volume where splays detach from the ATF (Mirabella et al., 2011). In order to investigate the complex tectonic setting of this area, the Altotiberina Near Fault Observatory (TABOO-NFO) was established (Caracausi et al., 2023; Chiaraluca et al., 2014, 2022). This geophysical infrastructure includes seismic, geodetic, geochemical, and meteorological sensors (Chiaraluca et al., 2014), recently enhanced with a STRainmeter ARray (STAR) of six Gladwin Tensor StrainMonitor (GTSM, Chiaraluca et al., 2024). Using TABOO's dense geophysical network, we analyze the

© 2026. The Author(s).

This is an open access article under the terms of the [Creative Commons Attribution License](https://creativecommons.org/licenses/by/4.0/), which permits use, distribution and reproduction in any medium, provided the original work is properly cited.

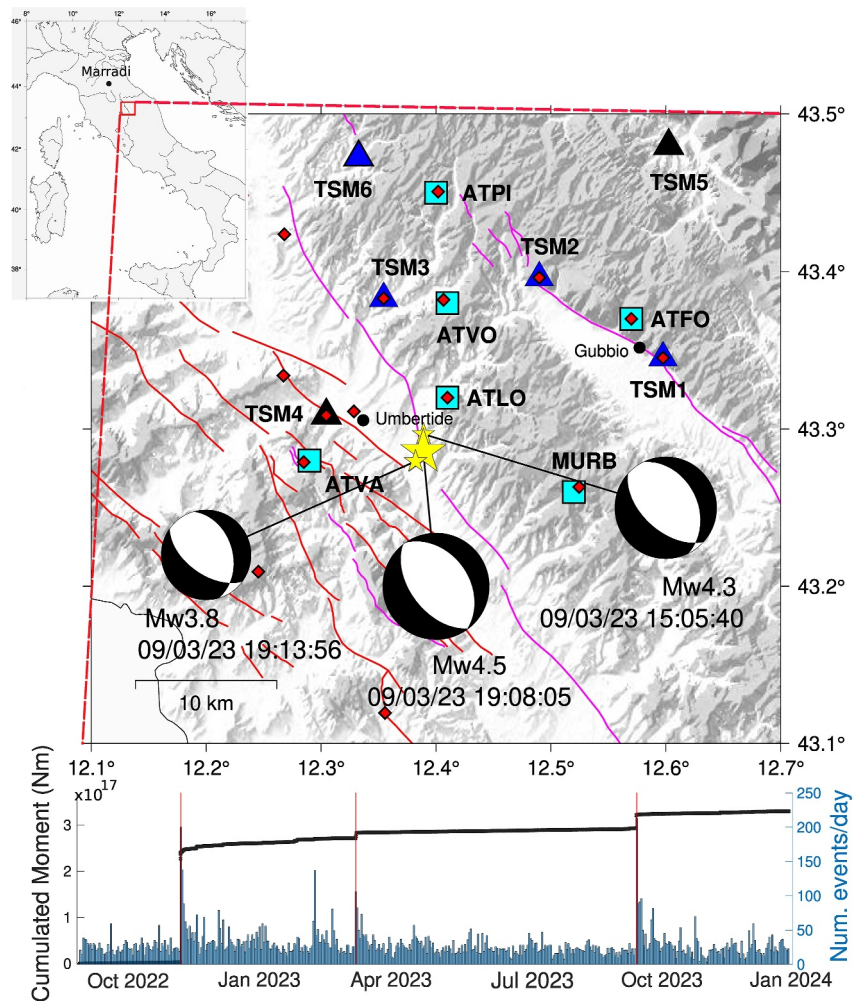


Figure 1. Map of the study area. Red and magenta lines mark the traces respectively of the E-dipping and W-dipping faults known in literature (Mirabella et al., 2011). Yellow stars show the location of the 3 events of March 9th (UTC time, focal mechanisms from ISIDE Working Group (2007)). Cyan squares indicate the seismometers employed in this study, red diamonds the GNSS stations within a radius of 20 km from the M_w 4.5 epicenter, triangles the strainmeter array (blue and black respectively those with and without data on March 9th). Bottom panel: cumulated seismic moment released and number of events per day for the events within a radius $R < 120$ km from Umbertide in the time span 1st of September 2022–31st of December 2023 (earthquakes from ISIDE Working Group (2007)). Red vertical lines mark respectively the 9/11/2022 M_w 5.2–5.5 Costa Marchigiana earthquakes, the March 9th 2023 earthquakes and the 18/09/2023 Marradi M_w 4.9 earthquake.

March 9th seismic sequence with ambient seismic noise cross-correlation, measuring seismic wave travel time variations and relative velocity changes ($\frac{dv}{v}$). We focus on coda waves, which are highly sensitive to small crustal changes (Zaccarelli et al., 2011). This technique has been widely used for monitoring seismogenic faults (Brenquier et al., 2008; Poupinet et al., 1984), volcanic areas (Brenquier et al., 2014; Sens-Schönfelder & Wegler, 2006), and environmental variations (Hillers et al., 2015b; Meier et al., 2010). We complement seismic data with the available geodetic observations (Figure 1) and we investigate the impact of crustal fluids on the seismic sequence, as fluid-filled cracks can play a critical role in generating deformation patterns and inducing changes in crustal properties (De Lorenzo & Trabace, 2011; Pastori et al., 2012; Poli et al., 2020). Integrating pore pressure data with seismo-geodetic observations we can thus interpret the seismic sequence, demonstrating how multidisciplinary approaches may clarify the mechanisms behind low-energy earthquakes.

The paper is organized as follows: Section 2 describes data processing, results are presented in Section 3 and discussed in Section 4. Conclusions are drawn in Section 5.

2. Data Analysis

For the seismic noise analysis, we select broadband seismometers from the Italian National Seismic Network (INSN, <http://www.fdsn.org/networks/detail/IV/>) located within a 20 km radius of the M_w 4.5 epicenter. The analysis spans 16 months, from September 1st 2022 to December 31st 2023. After excluding stations with missing recordings during the days of interest, the network includes the six seismometers shown in Figure 1.

As detailed in Section S1 of Supporting Information S1, GNSS is unable to resolve sub-daily deformation associated with the Umbertide earthquakes and is therefore excluded. Instead, we leverage the newly installed GTSMs (Chiaraluca et al., 2024), capable of measuring horizontal strain components with high precision (10^{-11} strain, Gladwin, 1984) over time scales from seconds to months, largely outperforming GNSS (Reuveni et al., 2012). The GTSMs' high temporal resolution and precision allows us to detect geodetic strain from small seismic events that would otherwise remain undetected. Of the six strainmeters installed, four (TSM1, 2, 3, 6) were operational on March 9th and are used here (Figure 1).

2.1. Seismic Data Processing

We process and filter the raw hourly seismic data following these steps. First, we merge daily streams, linearly interpolating gaps <20% (Zaccarelli et al., 2011), while days with larger gaps are considered as missing data. Following prior studies (e.g., Shapiro et al., 2006; Zaccarelli et al., 2011), we apply spectral whitening in the 0.1–1 Hz band to account for oceanic microseisms and use a water-level iterative normalization in the time domain, which has proven to be less aggressive than the 1-bit normalization (Bensen et al., 2007). 1-hour data chunks of the different station pairs are cross-correlated to get daily cross-correlations (CCs). Despite many authors have succeeded in tracking $\frac{dv}{v}$ stacking the ZZ of CCs only, in order to get more stable results, we stack the CC from EE, NN, and ZZ receivers components. To calculate relative velocity variations $\frac{dv}{v}$, we adopt the Moving Window Cross Spectral (MWCS) technique (Poupinet et al., 1984), applied to CC codas as in Brenguier et al. (2008); Clarke et al. (2011). This method estimates the relative time lag ($\frac{dt}{t}$) by performing linear regression in the phase-frequency domain between a reference cross-correlation (CC_{ref}) and the current cross-correlation (CC_{cur}). Under the assumption of perturbations acting homogeneously on the sampled volume, the relative velocity variations are (Poupinet et al., 1984):

$$\frac{dt}{t} = -\frac{dv}{v} \quad (1)$$

CC_{ref} is obtained by stacking all CC over the entire study period for each station pair and component. CC_{cur} are obtained by stacking data over a 25-day moving window with a 1-day step. The 25-day window provides the best balance between a high correlation coefficient ($r > 80\%$) and adequate sensitivity to variations (see Section S2 in Supporting Information S1). Using the MWCS approach on CC codas ensures a thorough sampling of the crustal volume due to the multiple scattering of surface waves. However, the actual part of the CC representing the coda is not univocally defined. In this paper codas are defined as starting from the theoretical arrival time of surface waves, estimated assuming a phase velocity $v_s = 2$ km/s of the Rayleigh waves that propagate within the upper crust (Moretti et al., 2009), and ending based on the Root Mean Square (RMS) of CC_{ref} as detailed in Supplementary (Section S3 in Supporting Information S1). The $\frac{dv}{v}$ are then obtained by stacking EE, NN, ZZ CC for each station pair, sampling the crustal volume down to ~ 5 km depth (based on surface wave penetration at these frequencies, Almagro Vidal et al., 2024). Results are shown in Figure 2a.

2.2. Strain Data Processing

Strain data for the 9th of March have been downloaded using the EarthScope strain tool (<https://earthscopestraintools.readthedocs.io/en/latest/>), and we downsample at 1 min the original 1 Hz record. Provided that we consider the full day of the events, data processing includes the correction for the long term drift and the removal of tidal-related strains. After a visual comparison among barometric and strain time series, and due to the small atmospheric pressure variations ($\lesssim 1$ hPa) recorded on that day, we neglect the influence of barometric pressure on strain data and we do not correct for them, as we expect atmospheric-related deformations ~ 1 nstrain (Roeloff, 2010). Before strain data can be incorporated into any geophysical model, the assessment of the instrument response, that is calibration, which relates the raw measurements to the regional crustal strain field, is mandatory.

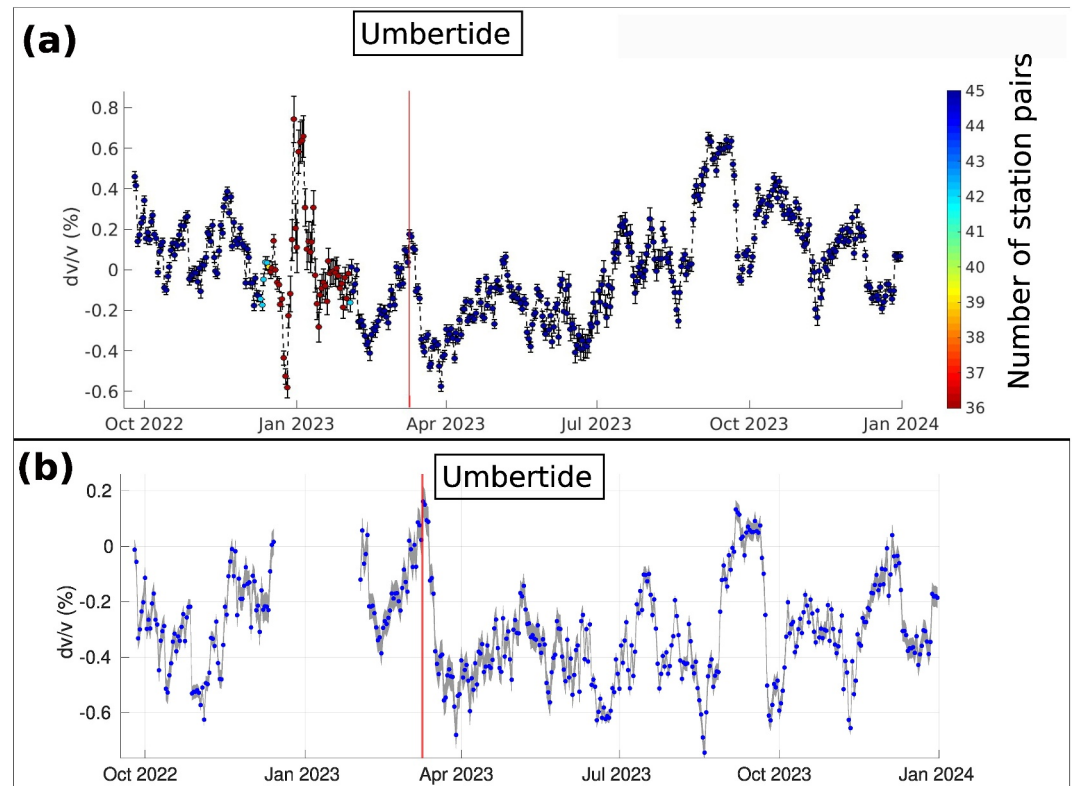


Figure 2. (a) Relative velocity variation in the time span analyzed. Color palette defines the number of station pairs stacked. (b) Relative velocity variation after the correction for temperature and rain (Section 2.1). The period between December 15th and February 3rd, when the $\frac{dv}{v}$ is not well constrained, has been removed from the time series. Gray shaded area show uncertainties. Red vertical line marks the epoch of the Umbertide earthquakes.

Calibration of the STAR array is described in a dedicated paper (Hanagan et al., 2025), and in particular we adopt the approach reported in Supplemental Text B of Hanagan et al. (2025) which follows the methodology of Mandler et al. (2024). Calibration matrices used in this work are reported in Supplementary (Table S1 in Supporting Information S1) for simplicity. The deployed borehole strainmeter instruments provide information about the horizontal strain field:

$$\epsilon = \begin{pmatrix} \epsilon_{EW} & \epsilon_{SWEN} \\ \epsilon_{SWEN} & \epsilon_{NS} \end{pmatrix} \quad (2)$$

However, GTSMs do not directly measure the strain tensor components, but the linear strain in four non-aligned channels. From their combination, it is possible to measure the areal ($AR = \epsilon_{EW} + \epsilon_{NS}$), differential ($ED = \epsilon_{EW} - \epsilon_{NS}$) and engineering ($ES = 2\epsilon_{SWEN}$) strain, which ultimately can be converted in E, N, and EN components if needed. As an example, the processing of the 1 Hz daily time series for TSM1 is provided in Supplementary (Section S4 in Supporting Information S1), whereas processing results for the four GTSMs are shown in Figures 3a–3d and they will be better explored in Section 3.2.

3. Results

3.1. Seismic Data Results

Figure 2a shows highly unstable velocity variations between mid-December 2022 and February 2023, which we attribute not to actual crustal velocity changes but to the reduced number of available station pairs (indicated by hot colors in Figure 2a). This limitation results in less constrained $\frac{dv}{v}$ measurements, as evident from the larger associated error bars. To ensure more reliable interpretations, we restrict our analysis to periods with at least 40

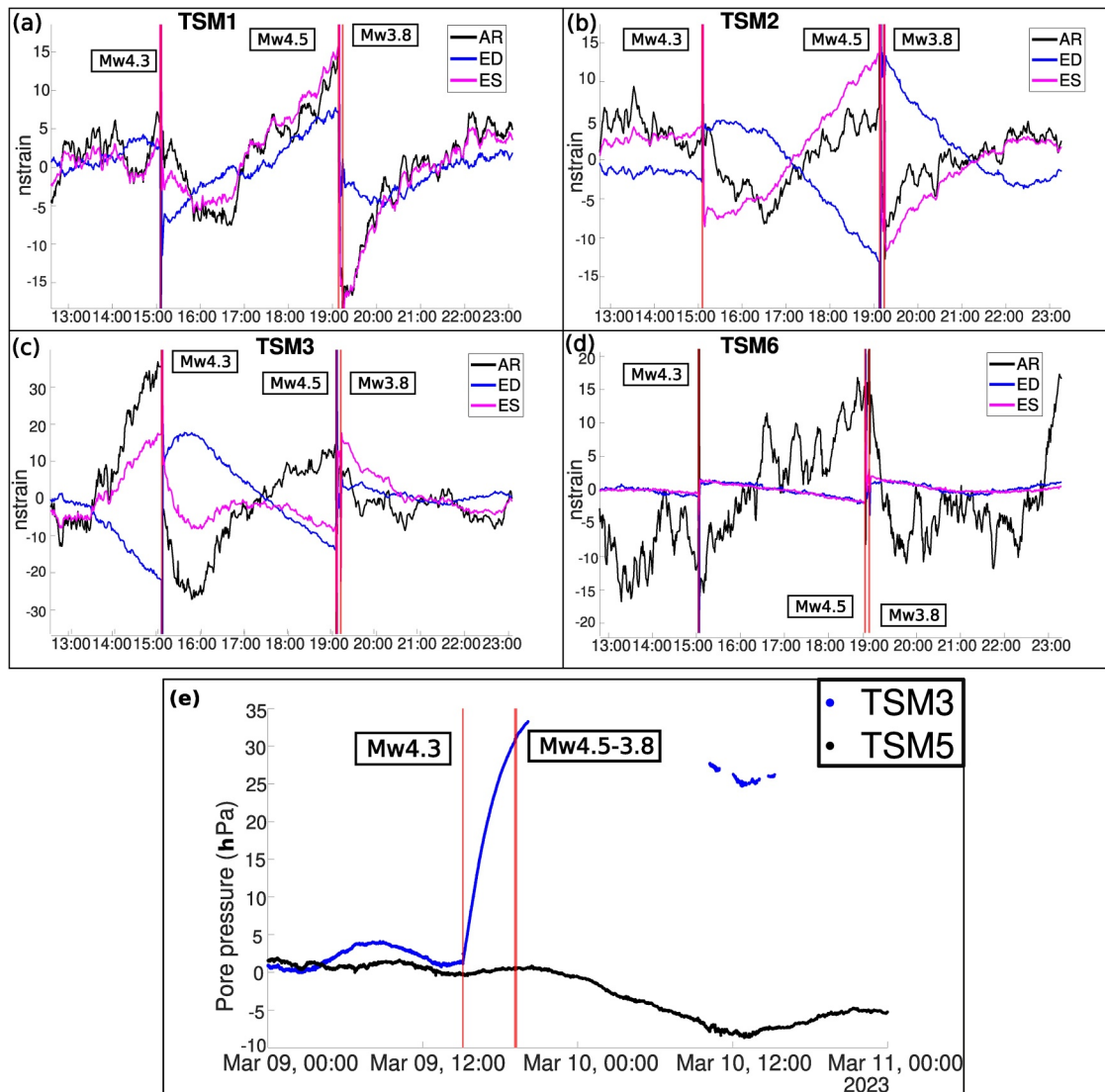


Figure 3. 1 min sampled areal (AR, black), differential (ED, blue), engineering (ES, magenta) strain time series for (a) TSM1, (b) TSM2, (c) TSM3 and (d) TSM6. Red vertical lines mark the M_w 4.3 15:05, M_w 4.5 19:08 and M_w 3.8 19:13 UTC earthquakes. Panel (e) shows the pore pressure variations measured at TSM3 (blue) and TSM5 (black).

station pairs. Notably, Figure 2a reveals a sudden drop in $\frac{dv}{v}$ during the Umbertide seismic sequence (March 2023), with a delay caused by the 25-day stacking. Since $\frac{dv}{v}$ can also be influenced by seasonal and meteorological effects (Almagro Vidal et al., 2021), we compare our time series with mean temperature ($T(t)$) and cumulated and detrended rainfall ($R(t)$) data from 13 nearby sites (Table S2 in Supporting Information S1) to remove nontectonic contributions. Stacked and detrended temperature and rainfall data are shown in Figure S5a of Supporting Information S1. We correlate $R(t)$ and $\frac{dv}{v}(t)$ and we get a maximum correlation coefficient ~ -0.44 with a zero time lag. Anticorrelation is expected since an increase in water content in the crust is generally associated with a decrease of $\frac{dv}{v}$ (e.g., Almagro Vidal et al., 2021). Comparison between $T(t)$ and $\frac{dv}{v}(t)$ gives a maximum correlation coefficient 0.26 with a 43 days time delay. Such a time delay between $T(t)$ and $\frac{dv}{v}(t)$ may be explained as due to the time necessary for temperature to warm up and deform the thermal boundary layer thickness, y_b , as defined in Berger (1975). Considering a 43 days delay we get $y_b \sim 2.1$ m, which is consistent with the characteristic thickness of the layer where temperature is dissipated (Berger, 1975).

Given the influence of the environmental forcing on velocity variations we proceed to their removal as in Mikhael et al. (2024), namely we produce some synthetic $\frac{dv}{v}_{syn}$:

$$\frac{dv^T}{v}_{syn}(t) = \left\langle \frac{dv}{v}(t) \right\rangle + \left(\frac{cov(\frac{dv}{v}, T)}{var(T(t))} \right) T(t) \quad (3)$$

$$\frac{dv^R}{v}_{syn}(t) = \left\langle \frac{dv}{v}(t) \right\rangle + \left(\frac{cov(\frac{dv}{v}, R)}{var(R(t))} \right) R(t) \quad (4)$$

where $\langle . \rangle$ stands for the temporal mean, $cov()$ and $var()$ respectively the covariance and variance among the indicated quantities. Slope derived from Equation 3 for $\frac{dv^T}{v}_{syn}(t)$ is $\sim 1.8 \times 10^{-4}$, whereas slope for $\frac{dv^R}{v}_{syn}(t) \sim -2.5 \times 10^{-5}$, therefore temperature seems to be the main environmental source causing velocity variations in the area and period considered (Figure S5 in Supporting Information S1), even though precise disentangling of environmental forcings with similar temporal evolution may prove difficult, as already observed in GNSS data (e.g., Laroche et al., 2018).

Figure 2b shows $\frac{dv}{v}$ after removing the temperature and rain effects and we can more clearly identify the drop relative to the Umbertide seismic sequence, with a significantly large decrease of $\sim 0.6\%$. We observe a $\frac{dv}{v} \sim 0.4\%$ surge around the end of August 2023 followed by a second drop on the 20th of September 2023 which is visible also in Figure 2a, and it is even more evident after the removal of the effects of rainfall and temperature. In order to define which variations of $\frac{dv}{v}$ are significantly out of the error, and to estimate measurements variability, we assume normally distributed data and we fix a 2σ threshold to evaluate their significance, finding that only the drop around the Umbertide earthquakes and the above mentioned surge in August overcome this threshold (Figure S12 in Supporting Information S1). Despite the drop \sim September 20th comes out to be within the statistical variability of our time-series, we deem it worth discussing as it occurs only 2 days after a M_w 4.9 earthquake with epicenter almost 100 km apart toward NW (close to the Marradi village, in the Mugello basin, Tuscany, Figure 1). However, no evidence has stood out to support the hypothesis of a causal link between the Marradi earthquake and the observed $\frac{dv}{v}$, therefore we neglect possible relationships. Further details about the drop around September 20th, as well as on the other changes, will be provided in Section S11 of Supporting Information S1.

We can compare the $\frac{dv}{v}$ associated with the Umbertide earthquakes and the dynamic strain ϵ_d induced in the rock's volume through the dynamic strain sensitivity β (Hillers et al., 2015a; Ostrovsky & Johnson, 2001):

$$\frac{dv}{v} = \beta \epsilon_d \quad (5)$$

where β represents a second-order quadratic term of the rocks' constitutive law (e.g., Delorey et al., 2021; Poli et al., 2020). To compute ϵ_d from seismic traces, we follow the approach of Gomberg and Agnew (1996), according to which

$$\epsilon_d^{seism} = \frac{PGV}{v_s} \quad (6)$$

The Peak Ground Velocity PGV, averaged over the seismic network and components (Section S6 in Supporting Information S1), gives a peak velocity ~ 1.2 cm/s (Figure S6 in Supporting Information S1) and therefore a $\epsilon_d^{seism} \sim 6 \mu strain$ ($v_s \sim 2$ km/s, Moretti et al., 2009). An independent assessment of the dynamic strain comes from the inspection of 1 Hz strainmeter time series, by using the RMS of the measured strain components (Barbour & Crowell, 2017):

$$\epsilon_d^{strainmeter} = \sqrt{(\epsilon_{xx}^2 + \epsilon_{yy}^2 + \epsilon_{xy}^2)/3} \quad (7)$$

$\epsilon_d^{strainmeter} \sim 0.1\text{--}1 \mu\text{strain}$, consistent with previous studies (Barbour & Crowell, 2017). Having $\epsilon_d \sim 10^{-5}\text{--}10^{-7}$ and a coseismic velocity drop $\frac{dv}{v}^{Umb} \sim -10^{-3}$ we find, from Equation 5, values of $\beta \sim -10^2; -10^4$. Further discussions will follow in Section 4.

3.2. Deformation Modeling

Strain time series resulting from the processing described in Section 2.2 and associated with the three 9th of March earthquakes for TSM1, TSM2, TSM3, TSM6 are shown in Figures 3a–3d.

Figures 3a–3d shows that areal deformations (AR, black lines) are coherently non-expansive for all of the sites and earthquakes, with static offsets reaching a maximum of $\sim 10 \text{ nstrain}$. On the other hand, shear deformations (differential strain ED, blue, and engineering strain ES, magenta) are more heterogeneous depending on the strainmeter position relative to the epicenters as well as on the event considered, and amplitudes are fastly dampened moving away from the epicenter (TSM6, Figure 3d).

The temporal evolution of deformation after the M_w 4.3 highlights some interesting differences among the sites, with TSM6 showing a monotonic areal expansion of $\sim 30 \text{ nstrain}$, whereas TSM3, TSM2, TSM1 show a quick areal relaxation after the co-seismic drop lasting respectively $\sim 60, 90, 100 \text{ min}$, followed by expansion until the M_w 4.5.

Post-seismic deformation is known to be primarily driven by elastic stress relaxation, poroelastic fluid redistribution, and viscoelastic relaxation in the crust and upper mantle (e.g., Fialko, 2004; Mandler et al., 2021; Perfettini & Avouac, 2007; Pollitz et al., 2000). Here, we exclude viscoelastic processes due to the small size of the seismic events, and we implement a forward poroelastic numerical model through the PEGRN-PECMP routine (R. Wang & Kumpel, 2003). This approach allows us to model the elastic (co-seismic + afterslip) and the poroelastic deformations, together with the relative pore pressure changes in a water saturated half space (Nespoli et al., 2025). To model the co-seismic deformation, we use the fault geometry of the ATF's synthetic splay, as obtained by preliminary inversion of InSAR ground displacements (Atzori et al., 2023, see insert of Figure 4a). A detailed description of the fault's parameters is reported in Table S3 of Supporting Information S1. We estimate the scalar moment M_0 through the relationship (Hanks & Kanamori, 1979):

$$M_0 = 10^{1.5 \times M_w + 9.1} \quad (8)$$

from which we derive the uniform slip $u \sim 5 \text{ mm}$ on the fault plane:

$$u = \frac{M_0}{\mu \times A} \quad (9)$$

where $\mu = 30 \text{ GPa}$ (consistent with Vadacca, 2020) is the rocks' shear modulus and A the slipping surface from Atzori et al. (2023). From Figure 4a, it is possible to notice that such a model gives areal contractions in the order of $\sim 1\text{--}10 \text{ nstrain}$ at the strainmeter sites, consistently both in sign and amplitude with the measured ones. To model the poroelastic post-seismic deformation, we impose the subsequent activation of rectangular fault planes extended 2.5 km along strike both northwards and southwards, and 2.5 km downdip of the co-seismic fault plane (Figure 4a, Table S4 in Supporting Information S1). We assume a ratio afterslip/coseismic moment = 30% (Avouac, 2015). Although for small earthquakes afterslip moment roughly equals the co-seismic moment (Gualandi et al., 2017; Hawthorne et al., 2016), Alwahedi and Hawthorne (2019) found an average post-seismic/co-seismic moment ratio $\sim 45\%$ in the 1.5 days after moderate (M 4 to 5) earthquakes. Since we are taking into account the first $\sim 4 \text{ hours}$ after the M_w 4.3, we assume a more conservative afterslip/co-seismic moment = 30%. Given the strong expansion measured at the strainmeter sites, following also previous authors (Nespoli et al., 2018), we maximize the poroelastic effects imposing a Skempton's coefficient $B = 1$, a Biot–Willis effective-stress coefficient $\alpha = 0.95$ and a hydraulic diffusivity $D = 1 \text{ m}^2/\text{s}$, which is a value representative of

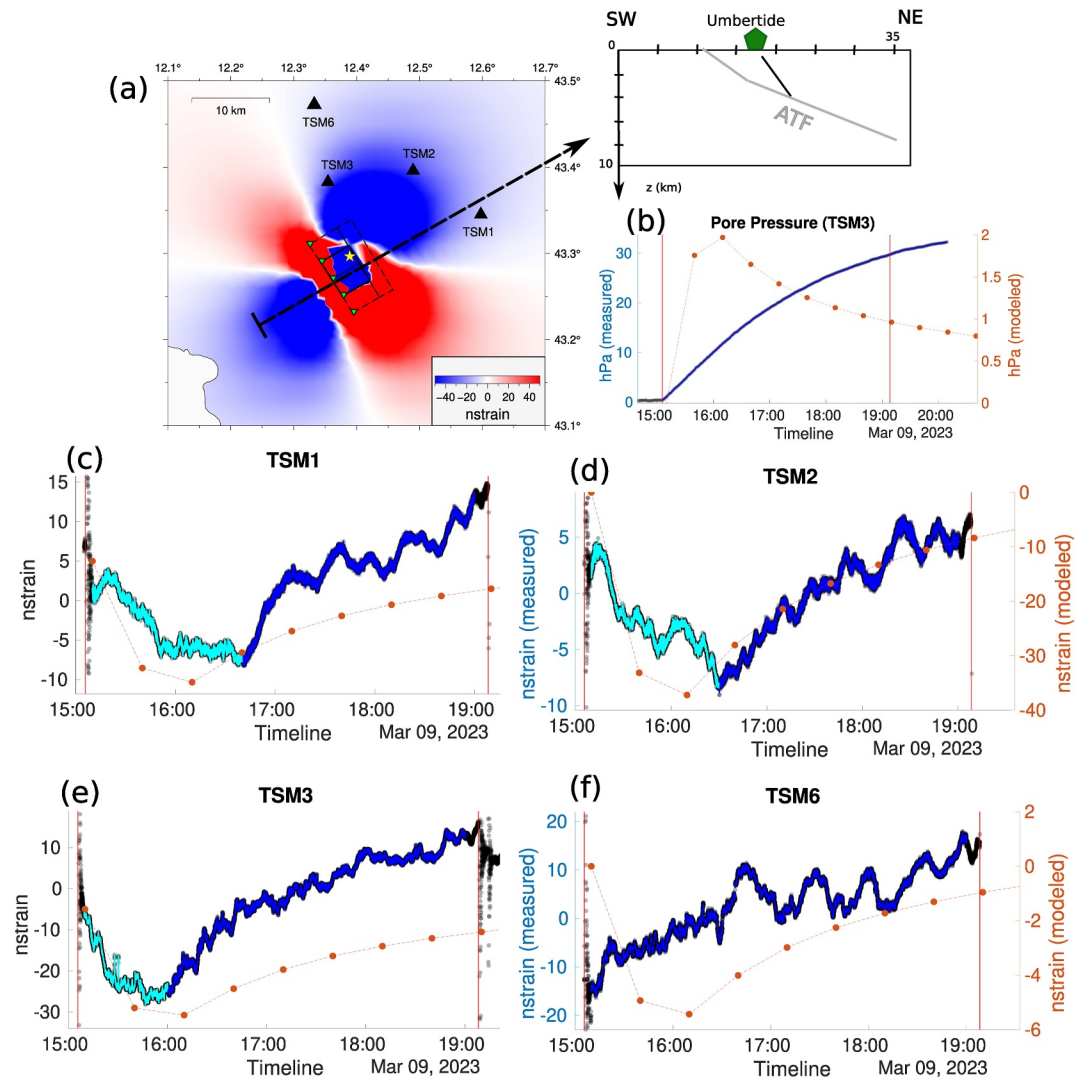


Figure 4. Poroelastic modeling of inter-events deformation. Panel (a): Areal coseismic deformation induced by the M_w 4.3 event (yellow star) modeled through the PEGRN-PECMP routine (blue compression, red expansion). Solid box shows the co-seismic fault plane, whereas dashed boxes show the fault planes used for the afterslip relaxation. Insert shows a cross-section of the map (ATF in light gray and the fault used to model the M_w 4.3 in black) along the SW-NE direction. Pentagon shows the position of Umbertide. Panel (b): Pore pressure measured at TSM3 site (blue). Panels (c–f): post-seismic areal strain time-evolution at respectively TSM1, 2, 3, 6. Cyan and blue curves show respectively the period when deformation is driven by afterslip and fluids. Orange markers show the model results. Note the different vertical scale panels (b, d, f).

the first few kilometers of the crust (e.g., Nespoli et al., 2018). Results of the post-seismic modeling are shown in Figures 4b–4f and will be discussed in Section 4.

4. Discussion

The analysis of continuous seismic records over a limited time span (16 months) and area (within 20 km from the epicenter of the M_w 4.5 event) allows us to clearly detect the crustal velocity drop associated with the low energy Umbertide seismic sequence. As previously shown (e.g., De Lorenzo & Trabace, 2011; Pastori et al., 2012), fluids-filled cracks at seismogenic depths are a major factor driving crustal velocity variations in the Apennines, which are also strongly influenced by the hydrological cycle (Hillers et al., 2015b; Wang et al., 2017). Conversely to Poli et al. (2020) and Almagro Vidal et al., 2024 we do not find variations in the water table and groundwater content due to seasonal effects to be the most influential factor. As a matter of fact we focus on a short time span (~ 1 year), during which temperature emerges as the dominant perturbing factor affecting the $\frac{dv}{v}$ (Section 2.1), as

found by Richter et al. (2014); Mikhael et al. (2024). The $\beta \sim -10^2; -10^4$ obtained from strain sensitivity analysis (Section 3.1) aligns with values reported in the literature (e.g., Takano et al., 2014; Yamamura et al., 2003). $\beta \neq 0$ is indicative of a departure from elastic linearity, and its magnitude reflects the level of crustal damage (Jin et al., 2018; Sens-Schönfelder et al., 2018). Specifically, $\beta < 0$ is interpreted as dilatation within the rock volume due to the re-opening of cracks, which is directly associated with a $\frac{dv}{v} < 0$ (Nur, 1971; Takano et al., 2019). Analyzing 1-min sampled strain data (Figure 3), we observe static strain offsets in the order of 10^0 – 10^1 *nstrain*, values that are 2–3 orders of magnitude smaller than dynamic ones. Hence, similarly to Brenguier et al. (2014), we attribute the observed velocity variations to the interaction between tectonically induced stress variations and crustal fluids.

Despite the low energy release of the Umbertide earthquakes, their associated velocity drop is clearly visible. As previous authors have shown (e.g., Brenguier et al., 2014; Zinszner et al., 1997), in regions where effective pressure is decreased by the presence of fluids, sensitivity of the seismic velocity is strongly affected. Analyzing the velocity variations at different depths (Figure S7 in Supporting Information S1), we notice that the drop corresponding to the Umbertide seismic sequence is more evident at frequency < 0.6 Hz (i.e., ~ 2 km depth), where highly pressurized CO_2 is known to be stored (e.g., Chiodini et al., 2004; Piana Agostinetti et al., 2017), and previous authors (e.g., Almagro Vidal et al., 2024) have already found evidence of coseismic crustal damaging enhanced by crustal fluids. Pore pressure measurements of sensors co-located with TSM3 and TSM5 (Figure 1) reveal a larger dynamic response at TSM3 after the M_w 4.3 and 4.5 events (Figure S8 in Supporting Information S1) and, more interestingly, a significant pore pressure increase of ~ 30 hPa, unseen by TSM5, in the time span between the two earthquakes with no significant static variation after the M_w 4.5 (Figure 3e). These observations lead us to investigate the poroelastic effects after the M_w 4.3 earthquake. The model in Section 3.2 offers insights into the processes acting after the M_w 4.3 (Figures 4b–4f): (a) coherently with the data, we observe limited co-seismic pore pressure variations at TSM3 (Figure 4b); (b) afterslip relaxation is needed to explain the rapid contraction at TSM1, TSM2, and TSM3, while TSM6 seems to be more influenced by fluids effects (Figures 4c–4f); (c) poroelastic effects can explain the post-seismic deformation at TSM1 and TSM3 (Figures 4c and 4d), and they account for $\sim 7\%$ of TSM3's pore pressure increase (Figure 4b). However, the high hydraulic diffusivity necessary to maximize areal expansion fails to replicate TSM3's temporal pore pressure evolution (Figure 4b). Tests with higher diffusivity ($D = 10 \text{ m}^2/\text{s}$) or increased afterslip moment ratios (100%) fail at better explaining the measured post-seismic deformation, as discussed in Section S9 in Supporting Information S1. Interestingly, stress induced by the poroelastic relaxation during the ~ 4 hours separating the earthquakes has positively recharged the area that ruptured during the M_w 4.3 of a few kPa (Figure S11 in Supporting Information S1). Despite the low stress increase predicted by the model, we can infer a possible role of fluids in triggering the M_w 4.5. Further details are reported in Section S9 in Supporting Information S1.

Results of the model suggest a limited contribution of the poroelastic mechanism to the strain measured at the borehole sites, meaning that fluids diffusing from the hypocentral area can explain only partially the observed deformation. A possible explanation to the post-seismic pattern comes from the enhanced permeability model firstly proposed by Roeloff (1998), according to which the passage of the seismic waves may cause, in the intermediate field, a gradual but sustained water level change (C. Wang & Chia, 2008). Brodsky et al. (2003) suggest that highly fractured media may be clogged with time by colloidal flocs. The ground shaking induced by the passage of seismic waves may disaggregate the flocs which loose their effects on permeability. A gradual pore pressure change, rather than a step-like variation, implies that barriers are formed not immediately in the proximity of the borehole (Brodsky et al., 2003), as the enhanced permeability likely connects the borehole to a close-by pressure source which requires time to transmit the pore pressure perturbation (Wang & Chia, 2008). Similar velocity drops have already been associated with cracks re-opening and permeability increase by Brenguier et al. (2014). Pore pressure variations at TSM3 following the February 6th M_w 7.8 Turkey-Syria earthquake resemble those seen in the Umbertide sequence (Figure S9 in Supporting Information S1), which supports the hypothesis of an earthquake enhanced permeability. According to Roeloff (1998), the sign of pore pressure perturbation will be the same (either positive or negative) independently of the earthquake source, as it is the case here.

5. Conclusive Remarks

We shed new light on the complex interplay between seismic wave propagation, crustal damage, and fluid dynamics during a low-energy seismic sequence. Despite the moderate magnitude of the earthquakes considered ($M_w \leq 4.5$), in fact, we detect a clear coseismic reduction in seismic velocity, indicating transient crustal damage amplified by the presence of fluids. By integrating seismic ambient noise monitoring, high-resolution borehole strainmeter and pore pressure measurements, we find that post-seismic deformation following the first event was driven not only by elastic afterslip, but also by fluid diffusion and transient stress redistribution. The observed patterns suggest an increase in crustal permeability, likely induced by dynamic shaking, which may have facilitated fluid migration and modulated stress conditions within the fault zone. These findings point toward a potential triggering role of fluid overpressure and enhanced permeability, even in low-energy seismic sequences. Near-fault multidisciplinary observations are key in revealing subtle physical processes that influence fault behavior. In fluid-rich fault systems, such as the ATF, these processes may significantly contribute to the local stress budget and future studies should evaluate the role of fluid-induced stress redistribution in seismic hazard models.

Conflict of Interest

The authors declare no conflicts of interest relevant to this study.

Data Availability Statement

Raw seismic traces are provided by the Italian National Seismic Network (INSN, <http://www.fdsn.org/networks/detail/IV/>). Strain and pore pressure data are made available through Earthscope Data Services at the website <https://www.unavco.org/data/strain-seismic/bsm-data/bsm-data.html>, and can be obtained through the Python package earthscopestraintool (<https://earthscopestraintools.readthedocs.io/en/latest/>). Relative velocity variations, strain time series, GNSS time series, the mean temperature and rainfall data used in this article are available on Zenodo (Mandler, E., 2025). GNSS time series are available on Zenodo at <https://doi.org/10.5281/zenodo.15240216>. Post-seismic deformation has been modeled using the PEGRN-PECMP software (C. Wang & Chia, 2008). The maps have been made using the GMT software (Wessel et al., 2019).

References

- Almagro Vidal, C., Zaccarelli, L., Pintori, F., Bragato, P. L., & Serpelloni, E. (2021). Hydrological effects on seismic-noise monitoring in karstic media. *Geophysical Research Letters*, 48(15), e2021GL093191. <https://doi.org/10.1029/2021GL093191>
- Almagro Vidal, C., Zaccarelli, L., Pintori, F., & Serpelloni, E. (2024). Crustal deformation and seismic velocity perturbations in the Alto Tiberina fault zone (Northern Apennines, Italy). *Journal of Geophysical Research: Solid Earth*, 129(11), e2024JB029023. <https://doi.org/10.1029/2024JB029023>
- Alwahedi, M. A., & Hawthorne, J. C. (2019). Intermediate-magnitude postseismic slip follows intermediate-magnitude (M 4 to 5) earthquakes in California. *Geophysical Research Letters*, 46(7), 3676–3687. <https://doi.org/10.1029/2018GL081001>
- Anderlini, L., Serpelloni, E., & Belardinelli, M. E. (2016). Creep and locking of a low-angle normal fault: Insights from the Altotiberina fault in the northern Apennines (Italy). *C. Geophys. Res. Lett.*, 43(9), 4321–4329. <https://doi.org/10.1002/2016GL068604>
- Atzori, S., Monterosso, F., Antonioli, A., De Luca, C., Sviggas, N., Casu, F., et al. (2023). Automatic seismic source modeling of InSAR displacements. *International Journal of Applied Earth Observation and Geoinformation*, 123, 103445. <https://doi.org/10.1016/j.jag.2023.103445>
- Avouac, J.-P. (2015). From geodetic imaging of seismic and aseismic fault slip to dynamic modeling of the seismic cycle. *Annual Review of Earth and Planetary Sciences*, 43(1), 233–271. <https://doi.org/10.1146/annurev-earth-060614-105302>
- Barbour, A., & Crowell, B. (2017). Dynamic strains for earthquake source characterization. *Seismological Research Letters*, 88(2A), 354–370. <https://doi.org/10.1785/0220160155>
- Bensen, G. D., Ritzwoller, M. H., Barmin, M. P., Levshin, A. L., Lin, F., Moschetti, M. P., et al. (2007). Processing seismic ambient noise data to obtain reliable broad-band surface wave dispersion measurements. *Geophysical Journal International*, 169(3), 1239–1260. <https://doi.org/10.1111/j.1365-246X.2007.03374.x>
- Berger, J. (1975). A note on thermoelastic strains and tilts. *Journal of Geophysical Research*, 80(2), 274–277. <https://doi.org/10.1029/JB080i002p00274>
- Brenguier, F., Campillo, M., Hadziioannou, C., Shapiro, N. M., Nadeau, R. M., & Larose, E. (2008). Postseismic relaxation along the San Andreas fault at Parkfield from continuous seismological observations. *Science*, 321(5895), 1478–1481. <https://doi.org/10.1126/science.1160943>
- Brenguier, F., Campillo, M., Takeda, T., Aoki, Y., Shapiro, N. M., Briand, X., et al. (2014). Mapping pressurized volcanic fluids from induced crustal seismic velocity drops. *Science*, 345(6192), 80–82. <https://doi.org/10.1126/science.1254073>
- Brodsky, E., Roeloffs, E., Woodcock, D., Gall, I., & Manga, M. (2003). A mechanism for sustained groundwater pressure changes induced by distant earthquakes. *Journal of Geophysical Research*, 108(B8), 2390. <https://doi.org/10.1029/2002JB002321>
- Caracausi, A., Camarda, M., Chiaraluce, L., De Gregorio, S., Favara, R., & Pisciotta, A. (2023). A novel infrastructure for the continuous monitoring of soil CO₂ emissions: A case study at the Alto Tiberina near fault observatory in Italy. *Front. Earth Sci.*, 11, 1172643. <https://doi.org/10.3389/feart.2023.1172643>
- Chiaraluce, L., Amato, A., Carannante, S., Castelli, V., Cattaneo, M., Cocco, M., et al. (2014). The Alto Tiberina near fault observatory (northern Apennines, Italy). *Annals of Geophysics*, 57(3), S0327. <https://doi.org/10.4401/ag-6426>

Acknowledgments

Open access funding provided by Istituto Nazionale di Geofisica e Vulcanologia within the CRUI-CARE Agreement. This work is supported by the INGV Departmental Strategic Project “Progetto Centro Italia DL50 - Monitoraggio sismico” and “MUSE.” Eugenio Mandler is supported by “Progetto Centro Italia DL50 - Monitoraggio sismico”. During this research L.C. has been partly supported by the European Research Council (ERC; Grant agreement 835012, TECTONIC). While TABOO-NFO is an infrastructural effort of the Italian Istituto Nazionale di Geofisica e Vulcanologia (Chiaraluce et al., 2014) whose raw data and scientific products are distributed through the European Near Fault Observatory community portals (Chiaraluce et al., 2022) implemented in the context of the EPOS consortium.

- Chiaraluce, L., Bennett, R., Mencin, D., Johnson, W., Barchi, M. R., Bohnhoff, M., et al. (2024). A strainmeter array as the fulcrum of novel observatory sites along the Alto Tiberina near fault observatory. *Scientific Drilling*, 33(2), 173–190. <https://doi.org/10.5194/sd-33-173-2024>
- Chiaraluce, L., Festa, G., Bernard, P., Caracausi, A., Carluccio, I., Clinton, J., et al. (2022). The near fault observatory community in Europe: A new resource for faulting and hazard studies. *Annals of Geophysics*, 65(3), DM316. <https://doi.org/10.4401/ag-8778>
- Chiodini, G., Cardellini, C., Amato, A., Boschi, E., Caliro, S., Frondini, F., & Ventura, G. (2004). Carbon dioxide Earth degassing and seismogenesis in central and southern Italy. *Geophysical Research Letters*, 31(7), L07615. <https://doi.org/10.1029/2004GL019480>
- Clarke, D., Zaccarelli, L., Shapiro, N., & Brenguier, F. (2011). Assessment of resolution and accuracy of the moving window cross spectral technique for monitoring crustal temporal variations using ambient seismic noise. *Geophysical Journal International*, 186(2), 1–16. <https://doi.org/10.1111/j.1365-246X.2011.05074.x>
- De Lorenzo, S., & Trabace, M. (2011). Seismic anisotropy of the shallow crust in the Umbria–Marche (Italy) region. *Physics of the Earth and Planetary Interiors*, 189(1–2), 34–46. <https://doi.org/10.1016/j.pepi.2011.09.008>
- Delorey, A. A., Guyer, R. A., Bokelmann, G. H. R., & Johnson, P. A. (2021). Probing the damage zone at Parkfield. *Geophysical Research Letters*, 48(13), e2021GL093518. <https://doi.org/10.1029/2021gl093518>
- Fialko, Y. (2004). Evidence of fluid-filled upper crust from observations of postseismic deformation due to the 1992 M_w 7.3 landers earthquake. *Journal of Geophysical Research*, 109, B08401. <https://doi.org/10.1029/2004JB002985>
- Gladwin, M. T. (1984). High precision multi component borehole deformation monitoring. *Review of Scientific Instruments*, 55(12), 2011–2016. <https://doi.org/10.1063/1.1137704>
- Gomberg, J., & Agnew, D. (1996). The accuracy of seismic estimates of dynamic strains: An evaluation using strainmeter and seismometer data from Piñon flat observatory, California. *Bulletin of the Seismological Society of America*, 86(1A), 212–220. <https://doi.org/10.1785/bssa08601a0212>
- Gualandi, A., Nichele, C., Serpelloni, E., Chiaraluce, L., Anderlini, L., Latorre, D., et al. (2017). Aseismic deformation associated with an earthquake swarm in the northern Apennines (Italy). *Geophysical Research Letters*, 44(15), 7706–7714. <https://doi.org/10.1002/2017GL073687>
- Hanagan, C., Mandler, E., Bennett, R., Chiaraluce, L., Gottlieb, M., Gualandi, A., et al. (2025). Characterization and validation of tidally calibrated strains from the Alto Tiberina near fault observatory strainmeter array (TABOO-NFO-STAR). *Seismica*, 4(1). <https://doi.org/10.26443/seismica.v4i1.1471>
- Hanks, T. C., & Kanamori, H. (1979). A moment magnitude scale. *Journal of Geophysical Research*, 84(B5), 2348–2350. <https://doi.org/10.1029/JB084iB05p02348>
- Hawthorne, J. C., Simons, M., & Ampuero, J.-P. (2016). Estimates of aseismic slip associated with small earthquakes near San Juan Bautista, CA. *Journal of Geophysical Research: Solid Earth*, 121(11), 8254–8275. <https://doi.org/10.1002/2016JB013120>
- Hillers, G., Ben-Zion, Y., Campillo, M., & Zigone, D. (2015a). In situ observations of velocity changes in response to tidal deformation from analysis of the high-frequency ambient wavefield. *Journal of Geophysical Research: Solid Earth*, 120, 210–225. <https://doi.org/10.1002/2014JB011318>
- Hillers, G., Ben-Zion, Y., Campillo, M., & Zigone, D. (2015b). Seasonal variations of seismic velocities in the San Jacinto fault area observed with ambient seismic noise. *Geophysical Journal International*, 202(2), 920–932. <https://doi.org/10.1093/gji/ggv151>
- ISIDe Working Group. (2007). *Italian seismological instrumental and parametric database (ISIDe)*. Istituto Nazionale di Geofisica e Vulcanologia (INGV). <https://doi.org/10.13127/ISIDE>
- Jin, J., Rivière, J., Ohara, Y., & Shokouhi, P. (2018). Dynamic acousto-elastic response of single fatigue cracks with different microstructural features: An experimental investigation. *Journal of Applied Physics*, 124(7), 075303. <https://doi.org/10.1063/1.5036531>
- Larochelle, S., Gualandi, A., Chanard, K., & Avouac, J.-P. (2018). Identification and extraction of seasonal geodetic signals due to surface load variations. *Journal of Geophysical Research: Solid Earth*, 123(12), 11031–11047. <https://doi.org/10.1029/2018JB016607>
- Mandler, E. (2025). Relative seismic velocity variations, strain time series, mean temperature and rainfall for the ATF area (September 2022 - December 2023) [Dataset]. *Zenodo*. <https://doi.org/10.5281/zenodo.15182917>
- Mandler, E., Canitano, A., Belardinelli, M. E., Nespoli, M., Serpelloni, E., & Linde, A. (2024). Tidal calibration of the Gladwin Tensor Strain Monitor (GTSM) array in Taiwan. *Pure and Applied Geophysics*, 182(3), 1001–1021. <https://doi.org/10.1007/s00024-024-03453-9>
- Mandler, E., Pintori, F., Gualandi, A., Anderlini, L., Serpelloni, E., & Belardinelli, M. E. (2021). Post-seismic deformation related to the 2016 Central Italy seismic sequence from GPS displacement time-series. *Journal of Geophysical Research: Solid Earth*, 126(9), e2021JB022200. <https://doi.org/10.1029/2021JB022200>
- Meier, U., Shapiro, N. M., & Brenguier, F. (2010). Detecting seasonal variations in seismic velocities within Los Angeles basin from correlations of ambient seismic noise. *Geophysical Journal International*, 181, 985–996. <https://doi.org/10.1111/j.1365-246X.2010.04550.x>
- Mikhael, N., Poli, P., & Garambois, S. (2024). Non-linear seismic velocity variations observed during a seismic swarm in the Alto Tiberina low angle normal fault from ambient noise correlation measurements. *Journal of Geophysical Research: Solid Earth*, 129(2), e2023JB028232. <https://doi.org/10.1029/2023jb028232>
- Mirabella, F., Brozzetti, F., Lupattelli, A., & Barchi, M. R. (2011). Tectonic evolution of a low-angle extensional fault system from restored cross-sections in the Northern Apennines (Italy). *Tectonics*, 30(6), TC6002. <https://doi.org/10.1029/2011TC002890>
- Moretti, M., De Gori, P., & Chiarabba, C. (2009). Earthquake relocation and three-dimensional Vp and Vp/Vs models along the low angle Alto Tiberina Fault (Central Italy): Evidence for fluid overpressure. *Geophysical Journal International*, 176(3), 833–846. <https://doi.org/10.1111/j.1365-246X.2008.03984.x>
- Nespoli, M., Belardinelli, M. E., Gualandi, A., Serpelloni, E., & Bonafede, M. (2018). Poroelasticity and fluid flow modeling for the 2012 Emilia-Romagna earthquakes: Hints from GPS and InSAR data. *Geofluids*, 2018(1), 4160570. <https://doi.org/10.1155/2018/4160570>
- Nespoli, M., Yu, H., Rinaldi, A. P., Harrington, R., Belardinelli, M. E., Martinelli, G., & Piombo, A. (2025). Applications and future developments of the (thermo-) poro-elastic theory in geophysics. *Earth-Science Reviews*, 260(2025), 104996. <https://doi.org/10.1016/j.earscirev.2024.104996>
- Nur, A. (1971). Effects of stress on velocity anisotropy in rocks with cracks. *Journal of Geophysical Research*, 76(8), 2022–2034. <https://doi.org/10.1029/jb076i008p02022>
- Ostrovsky, L. A., & Johnson, P. A. (2001). Dynamic nonlinear elasticity in geomaterials. *La Rivista del Nuovo Cimento*, 24(7), 1–46. <https://doi.org/10.1007/bf03548898>
- Pastori, M., Valoroso, L., Piccinini, D., Wustfield, A., Zaccarelli, L., Bianco, F., et al. (2012). Crustal fracturing and presence of fluid as revealed by seismic anisotropy: Case histories from seismogenic areas in the Apennines (Italy). *Bollettino di Geofisica Teorica ed Applicata*, 2012.
- Pauselli, C., Barchi, M. R., Federico, C., Magnani, M. B., & Minelli, G. (2006). The crustal structure of the Northern Apennines (Central Italy): An insight by the CROP03 seismic line. *American Journal of Science*, 306(6), 428–450. <https://doi.org/10.2475/06.2006.02>

- Perfettini, H., & Avouac, J.-P. (2007). Modeling afterslip and aftershocks following the 1992 Landers earthquake. *Journal of Geophysical Research*, *112*(B7), B07409. <https://doi.org/10.1029/2006JB004399>
- Piana Agostinetti, N., Giacomuzzi, G., & Chiarabba, C. (2017). Seismic swarms and diffuse fracturing within Triassic evaporites fed by deep degassing along the low-angle Alto Tiberina normal fault (central Apennines, Italy). *Journal of Geophysical Research: Solid Earth*, *122*(1), 308–331. <https://doi.org/10.1002/2016JB013295>
- Poli, P., Marguin, V., Wang, Q., D'Agostino, N., & Johnson, P. (2020). Coseismic velocity variation in the Region of L'Aquila from single station measurements and implications for crustal rheology. *Journal of Geophysical Research: Solid Earth*, *125*(7), e2019JB019316. <https://doi.org/10.1029/2019jb019316>
- Pollitz, F. F., Peltzer, G., & Bürgmann, R. (2000). Mobility of continental mantle: Evidence from postseismic geodetic observations following the 1992 Landers earthquake. *Journal of Geophysical Research*, *105*(B4), 8035–8054. <https://doi.org/10.1029/1999JB900380>
- Poupinet, G., Ellsworth, W. L., & Frechet, J. (1984). Monitoring velocity variations in the crust using earthquake doublets: An application to the Calaveras fault, California. *Journal of Geophysical Research*, *89*(B7), 5719–5731. <https://doi.org/10.1029/jb089ib07p05719>
- Reuveni, Y., Kedar, S., Owen, S. E., Moore, A. W., & Webb, F. H. (2012). Improving sub-daily strain estimates using GPS measurements. *Geophysical Research Letters*, *39*(11), L11311. <https://doi.org/10.1029/2012GL051927>
- Richter, T., Sens-Schönfelder, C., Kind, R., & Asch, G. (2014). Comprehensive observation and modeling of earthquake and temperature-related seismic velocity changes in northern Chile with passive image interferometry. *Journal of Geophysical Research: Solid Earth*, *119*(6), 4747–4765. <https://doi.org/10.1002/2013JB010695>
- Roeloffs, E. A. (1998). Persistent water level changes in a well near Parkfield, California, due to local and distant earthquakes. *Journal of Geophysical Research*, *103*(B1), 869–889. <https://doi.org/10.1029/97jb02335>
- Roeloffs, E. A. (2010). Tidal calibration of plate boundary observatory borehole strainmeters: Roles of vertical and shear coupling. *Journal of Geophysical Research*, *115*(B6), B06405. <https://doi.org/10.1029/2009JB006407>
- Sens-Schönfelder, C., Snieder, R., & Li, X. (2018). Model for nonlinear elasticity in rocks based on friction of internal interfaces and contact aging. *Geophysical Journal International*. <https://doi.org/10.1093/gji/ggy414>
- Sens-Schönfelder, C., & Wegler, U. (2006). Passive image interferometry and seasonal variations of seismic velocities at Merapi Volcano, Indonesia. *Geophysical Research Letters*, *33*, L21302. <https://doi.org/10.1029/2006GL027797>
- Serpelloni, E., Cavaliere, A., Martelli, L., Pintori, F., Anderlini, L., Borghi, A., et al. (2022). Surface velocities and strain-rates in the Euro-Mediterranean Region from massive GPS data processing. *Frontiers in Earth Science*, *10*, 907897. <https://doi.org/10.3389/feart.2022.907897>
- Shapiro, N. M., Ritzwoller, M. H., & Bensen, G. D. (2006). Source location of the 26 sec microseism from cross-correlations of ambient seismic noise. *Geophysical Research Letters*, *33*(18), L18310. <https://doi.org/10.1029/2006GL027010>
- Takano, T., Nishimura, T., Nakahara, H., Ueda, H., & Fujita, E. (2019). Sensitivity of seismic velocity changes to the tidal strain at different lapse times: Data analyses of a small seismic array at Izu-Oshima volcano. *Journal of Geophysical Research: Solid Earth*, *124*(3), 3011–3023. <https://doi.org/10.1029/2018jb016235>
- Takano, T., Nishimura, T., Nakahara, H., Ohta, Y., & Tanaka, S. (2014). Seismic velocity changes caused by the Earth tide: Ambient noise correlation analyses of small-array data. *Geophysical Research Letters*, *41*(17), 6131–6136. <https://doi.org/10.1002/2014GL060690>
- Vadacca, L. (2020). The altotiberina low-angle normal fault (Italy) can fail in moderate-magnitude earthquakes as a result of stress transfer from stable creeping fault area. *Geosciences*, *10*(4), 144. <https://doi.org/10.3390/geosciences10040144>
- Vadacca, L., Casarotti, E., Chiaraluce, L., & Cocco, M. (2016). On the mechanical behaviour of a low-angle normal fault: The Alto Tiberina fault (Northern Apennines, Italy) system case study. *Solid Earth*, *7*(6), 1537–1549. <https://doi.org/10.5194/se-7-1537-2016>
- Valoroso, L., Chiaraluce, L., Di Stefano, R., & Monachesi, G. (2017). Mixed-mode slip behavior of the Altotiberina low-angle normal fault system (Northern Apennines, Italy) through high-resolution earthquake locations and repeating events. *Journal of Geophysical Research: Solid Earth*, *122*(12), 10220–10240. <https://doi.org/10.1002/2017JB014607>
- Wang, C.-Y., & Chia, Y. (2008). Mechanism of water level changes during earthquakes: Near field versus intermediate field. *Geophysical Research Letters*, *35*(12), L12402. <https://doi.org/10.1029/2008GL034227>
- Wang, Q.-Y., Brenguier, F., Campillo, M., Lecointre, A., Takeda, T., & Aoki, Y. (2017). Seasonal crustal seismic velocity changes throughout Japan. *Journal of Geophysical Research: Solid Earth*, *122*(10), 7987–8002. <https://doi.org/10.1002/2017JB014307>
- Wang, R., & Kumpel, H.-J. (2003). Poroelasticity: Efficient modeling of strongly coupled, slow deformation processes in a multilayered half-space. *Geophysics*, *68*(2), 705–717. <https://doi.org/10.1190/1.1567241>
- Wessel, P., Luis, J. F., Uieda, L., Scharoo, R., Wobbe, F., Smith, W. H. F., & Tian, D. (2019). The generic mapping tools version 6. *Geochemistry, Geophysics, Geosystems*, *20*(11), 5556–5564. <https://doi.org/10.1029/2019GC008515>
- Yamamura, K., Sano, O., Utada, H., Takei, Y., Nakao, S., & Fukao, Y. (2003). Long-term observation of in situ seismic velocity and attenuation. *Journal of Geophysical Research*, *108*, 2317. <https://doi.org/10.1029/2002jb002005>
- Zaccarelli, L., Shapiro, N. M., Faenza, L., Soldati, G., & Michelini, A. (2011). Variations of crustal elastic properties during the 2009 L'Aquila earthquake inferred from cross correlations of ambient seismic noise. *Geophysical Research Letters*, *38*(L24304). <https://doi.org/10.1029/2011GL049750>
- Zinszner, B., Johnson, P. A., & Rasolofosaon, P. N. J. (1997). Influence of change in physical state on elastic nonlinear response in rock: Significance of effective pressure and water saturation. *Journal of Geophysical Research*, *102*(B4), 8105–8120. <https://doi.org/10.1029/96JB03225>

References From the Supporting Information

- Bower, D. R., & Heaton, K. C. (1978). Response of an aquifer near Ottawa to tidal forcing and the Alaskan earthquake of 1964. *Canadian Journal of Earth Sciences*, *15*(3), 331–340. <https://doi.org/10.1139/e78-039>
- Carminati, E., Toniolo Augier, F., & Barba, S. (2001). Dynamic modelling of stress accumulation in Central Italy: Role of structural heterogeneities and rheology. *Geophysical Journal International*, *144*(2), 373–390. <https://doi.org/10.1046/j.1365-246x.2001.00323.x>
- Collettini, C., & Barchi, M. R. (2002). A Low-Angle normal Fault in the Umbria Region (Central Italy): A mechanical model for the related microseismicity. *Tectonophysics*, *359*(1–2), 97–115. [https://doi.org/10.1016/S0040-1951\(02\)00441-9](https://doi.org/10.1016/S0040-1951(02)00441-9)
- Piccinini, D., Piana Agostinetti, N., Saccorotti, G., Fiaschi, A., Matassoni, L., & Morelli, M. (2014). Orogen-parallel variability in 3D seismicity distribution, Northern Apennines (Italy): Evidence for a slab tear fault? *Journal of Geodynamics*, *82*, 110–117. <https://doi.org/10.1016/j.jog.2014.09.005>
- Pondrelli, S., Visini, F., Rovida, A., D'Amico, V., Pace, B., & Meletti, C. (2020). Style of faulting of expected earthquakes in Italy as an input for seismic hazard modeling. *Natural Hazards and Earth System Sciences*, *20*(12), 3577–3592. <https://doi.org/10.5194/nhess-20-3577-2020>